STEADY AND TRANSIENT INFLOW DYNAMICS WITH ACTUATOR DISK VORTEX THEORY

MORTEN DINHOFF PEDERSEN

Department of Engineering Cybernetics,
Norwegian University of Science and Technology (NTNU),
O. S. Bragstads Plass 2D, 7034 Trondheim, Norway

Abstract. The actuator disk is a well known and widely used theoretical tool in wind engineering. This work proposes a new theory based on an actuator surface, capable of treating time-varying vectorial load distributions and yaw/pitch misalignment. A simplified representation of vortex motion is used to arrive at a tractable problem. The theory is not restricted to disks; arbitrary coplanar (optionally disjoint) actuator surfaces may be modeled. Some of the theoretical novelties used in the modeling includes use of the fractional Laplacian and extensive use of the Fourier transform on $\mathbb{R}^2$. Promising experimental validation based on pitch-step experiments at the Tjæreborg turbine are furnished. Comparisons are also made to existing methodologies. Analysis and numerical work shows that the model encapsulates Coleman's vortex theory.

1. Introduction

Let S represent a planar permeable surface capable of supporting a concentrated load distribution $\boldsymbol{F}$. This theoretical construct will be referred to as an *actuator surface*. The well known actuator *disk* specializes the surface to a circle $S = \{\boldsymbol{x} : |\boldsymbol{x}| \leq R\}$. As loads are applied on S the fluid reacts by generating an inflow $\boldsymbol{u}$ which is the quantity sought identified through the actuator surface model. The inflow is typically needed for the calculation of blade loads and attendant integral quantities such as torque, power and thrust.

Using an actuator disk in lieu of lifting lines or lifting surfaces often brings significant simplifications to the fluid mechanical problem. By adopting this simplification, methods such as momentum theory[Hansen, 2008], computational fluid dynamics [Sørensen et al., 1998, Spalart, 2003] or vortex theory [Conway, 1995, Branlard and Gaunaa, 2015] can be used to identify the inflow $\boldsymbol{u}$ on the disk. The unsteady problem often require specialized tools, even when simplified with an actuator disk. Few alternatives exist if computational efficiency and ease of analysis are important. The acceleration potential models exemplified in Van Bussel [1995] and Peters et al. [1989] are salient examples of such models. CFD analysis[Sørensen et al., 1998] or vortex filament codes [Leishman et al., 2002] may offer improved fidelity but come with a heavy computational burden and act as numerical "black box" models.

Control-theoretical work on wind turbines have motivated the development of a new type of model expressly suited for this purpose. In control engineering, a high premium is placed on simplicity, ease of simulation and analytical tractability. While the Generalized Dynamic Wake (GDW) model of Peters and coworkers [Peters et al., 1989] would appear like a suitable candidate for this application, the approach is tied to a particular series expansion for the three dimensional fields originating with Kinner [1936]. This formulation has been found cumbersome and difficult to use in the identification of exact results. The scope of the model presented in this work is similar to later incarnations of the GDW theory as described in Morillo and Peters [2002]. However, the underlying physical reasoning and modeling capabilities are different enough to qualify it as a new theory.

Rather than adopting a series expansion, an explicit two dimensional governing equation for the inflow process is uncovered. This equation does not appear in the literature, perhaps due to its somewhat exotic *fractional* nature. In its most basic form, the novel governing equation will read as

$$\dot{w}_n + U_n\sqrt{-\nabla^2}w_n = \frac{1}{2\rho}\sqrt{-\nabla^2}\Delta p \tag{1}$$

Here, w_n represents the normal inflow at the surface, U_n a vortex transport velocity defined normal to the surface whereas Δp denotes the normal load distribution due to a pressure jump. The so-called fractional Laplacian is symbolized by $\sqrt{-\nabla^2}$. It turns out that (1) is best classified as a fractional heat equation [Bucur and Valdinoci, 2016]. Heat equations are known to give rise to diffusive solutions spreading out as time proceeds. Fractional heat equations are no different in this regard. However, equations such as (1) are also *nonlocal* implying that nonadjacent points on an actuator surface may interact directly via $\sqrt{-\nabla^2}$. Phenomena of this kind occur in diverse areas such as geostrophic flow [Caffarelli and Vasseur, 2010] and quantum mechanics [Laskin, 2000].

The aim of this paper is to introduce a general variation of (1) capable of representing the inflow on an actuator surface under steady and transient loading, with a vectorial forcing $\boldsymbol{F}$ and non-axial convection $\boldsymbol{U}$. We borrow the terminology Actuator Disk Vortex Theory from Johnson [1994] because the theory describes vortex dynamics associated with forcing applied to a surface in the nominal shape of a disk.

E-mail address: morten.d.pedersen@ntnu.no.

† This document is a post-print of Pedersen [2019].

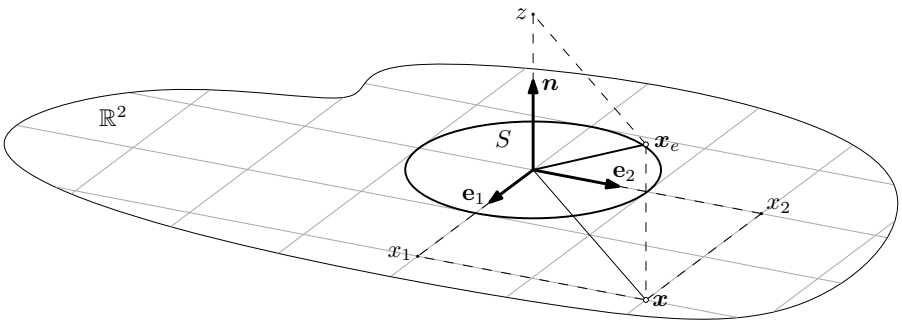

FIGURE 1. The actuator surface S embedded in $\mathbb{R}^2$ at $z = 0$. A disk-shaped special case is shown. Coordinates in the plane $\boldsymbol{x} \in \mathbb{R}^2$ extend with a vertical coordinate z to give the three dimensional coordinate $\boldsymbol{x}_e \in \mathbb{R}^3$. The face of S shown in the figure will be referred to as the upper/downstream face. On the other side one finds the lower/upstream face.

Since the new methodology is very general only select applications will be studied. Predictions under time-varying loads differ significantly from models based on the acceleration potential. This topic is given due attention in Section 3. On the other hand, Coleman theory [Coleman et al., 1945] with modern extensions in Branlard and Gaunaa [2016] is reproduced exactly. This will be demonstrated in Section 4. An assortment of plots will be presented; unless specified otherwise, the spectral numerical scheme detailed in Appendix B was used to generate the data.

2. MODELING

An inviscid and incompressible fluid residing in an unbounded volume is assumed. Consider Figure 1. A 2+1 spatial coordinate scheme is adopted where $\boldsymbol{x} \in \mathbb{R}^2$ describes coordinates on the actuator surface S. An extended coordinate vector $\boldsymbol{x}_e \in \mathbb{R}^3$ is used to indicate points off the surface.

$$\boldsymbol{x} := \begin{bmatrix} x_1 \\ x_2 \end{bmatrix}, \quad \boldsymbol{x}_e := \begin{bmatrix} \boldsymbol{x} \\ z \end{bmatrix} \tag{2}$$

It will be necessary to distinguish between the gradient with respect to $\boldsymbol{x}$ and the extended coordinate $\boldsymbol{x}_e$. To this end, let

$$\nabla := \begin{bmatrix} \frac{\partial}{\partial x_1} \\ \frac{\partial}{\partial x_2} \end{bmatrix}, \quad \nabla_e := \begin{bmatrix} \nabla \\ \frac{\partial}{\partial z} \end{bmatrix} \tag{3}$$

The components of the flow perturbation $\boldsymbol{u}$ and the vortex transport velocity $\boldsymbol{U}$ are denoted by

$$\boldsymbol{u} := \begin{bmatrix} u_1 \\ u_2 \\ u_n \end{bmatrix}, \quad \boldsymbol{U} := \begin{bmatrix} U_1 \\ U_2 \\ U_n \end{bmatrix} \tag{4}$$

The fluid-mechanical problem is described by the vorticity equation [Saffman, 1995]. Let the flow field in $\mathbb{R}^3$ be denoted by $\boldsymbol{u} = \boldsymbol{u}(\boldsymbol{x}_e, t)$ and let the attendant vorticity be symbolized by $\boldsymbol{\zeta} = \nabla_e \times \boldsymbol{u}$. Letting $\boldsymbol{U}$ serve as a vortex transport velocity one has

$$\frac{\partial \boldsymbol{\zeta}}{\partial t} + \frac{\partial \boldsymbol{\zeta}}{\partial \boldsymbol{x}_e}\boldsymbol{U} = \frac{\partial \boldsymbol{U}}{\partial \boldsymbol{x}_e}\boldsymbol{\zeta} + \frac{1}{\rho}\nabla_e \times \boldsymbol{f} \tag{5}$$

If a full nonlinear description of this problem was necessary, the vortex transport velocity would assume the form $\boldsymbol{U}(\boldsymbol{x}_e, t) = \boldsymbol{u}(\boldsymbol{x}_e, t) + \boldsymbol{U}_0(t)$ where $\boldsymbol{U}_0$ could be used to indicate an optional ambient flow field. Here, $\boldsymbol{U}$ will be understood as an averaged transport velocity representing the motion of vorticity confined to simplified wake structures. An opportune choice will be to interpret $\boldsymbol{U}$ as the sum of the free-stream and the averaged inflow at the surface S. Setting $\boldsymbol{U} = \boldsymbol{U}(t)$ allows the force field $\boldsymbol{f}$ to be related to a flow perturbation $\boldsymbol{u}$ in a simplified manner.

$$\frac{\partial \boldsymbol{\zeta}}{\partial t} + \frac{\partial \boldsymbol{\zeta}}{\partial \boldsymbol{x}_e}\boldsymbol{U} \simeq \frac{1}{\rho}\nabla_e \times \boldsymbol{f} \tag{6}$$

This equation is complemented by the Biot-Savart integral which yields $\boldsymbol{u}$ given $\boldsymbol{\zeta}$.

$$\boldsymbol{u} = \nabla_e \times \int_{\mathbb{R}^3} \frac{\boldsymbol{\zeta}'}{4\pi|\boldsymbol{x}_e - \boldsymbol{x}_e'|}\, d\boldsymbol{x}_e' \tag{7}$$

The force field is confined to the actuator surface located at $z = 0$. An appropriate description of this field is therefore furnished by

$$\boldsymbol{f}(\boldsymbol{x}_e, t) = \delta(z)\boldsymbol{F}(\boldsymbol{x}, t), \quad \boldsymbol{F} = \begin{bmatrix} \tau_1 \\ \tau_2 \\ \Delta p \end{bmatrix} \tag{8}$$

Here, $\delta(z)$ represents Dirac's delta-function. The force vector is populated by the tangential force distributions τ_1, τ_2 and the pressure jump Δp. The equations (6), (7) and (8) represent the inflow problem using three spatial coordinates and time. While one may proceed to solve the problem as it stands, drastic simplifications are possible.

The method proposed in this work converts the simplified 3D vortex transport equation (6) to a 2D fractional equation exemplified by (1). The price for this reduction in complexity is twofold. It must be assumed that the vortex transport velocity satisfies the following inequality

$$U_n = \boldsymbol{U} \cdot \boldsymbol{n} > 0 \tag{9}$$

This implies that vorticity will be confined to the *upper* half-space defined by $\mathbb{R}^3_+ := \{\boldsymbol{x}_e : z > 0\}$. Vorticity is generated at S and subsequently transported towards positive z. It is in fact possible to show that (1) will be unstable with $U_n < 0$. A second caveat is that information about the flow field in the upper half-space is lost. If these limitations are tolerable, the proposed model is suitable.

The new model consists of a state equation and a measurement equation together describing the flow perturbation $\boldsymbol{u}$ in the closed lower half-space $\bar{\mathbb{R}}^3_- := \{\boldsymbol{x}_e : z \leq 0\}$. These equations acquire their most convenient formulation in the Fourier-domain. The following convention will apply.

$$\hat{f}(\boldsymbol{k}) = \mathfrak{F}[f(\boldsymbol{x})] = \int_{\mathbb{R}^2} e^{-i\boldsymbol{k}\cdot\boldsymbol{x}} f(\boldsymbol{x})\ d\boldsymbol{x}, \quad f(\boldsymbol{x}) = \mathfrak{F}^{-1}[\hat{f}(\boldsymbol{k})] = \frac{1}{(2\pi)^2}\int_{\mathbb{R}^2} e^{i\boldsymbol{k}\cdot\boldsymbol{x}} \hat{f}(\boldsymbol{k})\ d\boldsymbol{k} \tag{10}$$

Let the normal flow at the actuator surface be denoted

$$w_n(\boldsymbol{x}, t) = \boldsymbol{n} \cdot \boldsymbol{u}(\boldsymbol{x}_e, t)|_{z=0} \tag{11}$$

The *state equation* describes the evolution of w_n. A Fourier domain representation reads as

$$\dot{\hat{w}}_n + (\hat{\boldsymbol{L}} \cdot \boldsymbol{U})\hat{w}_n = \frac{1}{2\rho}(\hat{\boldsymbol{L}} \cdot \hat{\boldsymbol{F}}) \tag{12}$$

Here, $\boldsymbol{L}$ denotes a 2D fractional formulation of the 3D gradient operator ∇_e. The fractional operator is equipped with representations in both Cartesian space and Fourier space, respectively given by

$$\boldsymbol{L} := \begin{bmatrix} \nabla \\ \sqrt{-\nabla^2} \end{bmatrix}, \quad \hat{\boldsymbol{L}} = \begin{bmatrix} i\boldsymbol{k} \\ |\boldsymbol{k}| \end{bmatrix} \tag{13}$$

More details will by given as the text proceeds. The flow field is extracted via a *measurement equation* given by

$$\hat{\boldsymbol{u}} = \frac{e^{|\boldsymbol{k}|z}}{|\boldsymbol{k}|}\hat{\boldsymbol{L}}\hat{w}_n + \frac{\Theta(z)}{\rho U_n}\begin{bmatrix} \hat{\tau}_1 \\ \hat{\tau}_2 \\ 0 \end{bmatrix} \tag{14}$$

In accordance with (10), the Fourier transform of $\boldsymbol{u}$ is taken with respect to the surface coordinate $\boldsymbol{x}$ leaving z in place. Heaviside's step function is defined according to the following convention

$$\Theta(z) := \begin{cases} 0 & z < 0 \\ 1/2 & z = 0 \\ 1 & z > 0 \end{cases} \tag{15}$$

Equations (12) and (14) embody (6), (7) and (8) but only apply in the closed lower half-space $\bar{\mathbb{R}}^3_-$ and subject to the inequality (9).

The modeling necessary to justify the new model given by (12) and (14) proceeds in three steps.

(1) In Section 2.1 the flow field at the lower face of the actuator surface is identified using potential flow in $\mathbb{R}^3_-$. Additional arguments involving the fractional Laplacian are invoked to accomplish a dimensional reduction from three spatial coordinates to two.
(2) A velocity jump is present at $z = 0$ due to the concentrated surface force (8). Simple conservation laws are used in Section 2.2 to identify this jump. Combining results from step 1 and 2 leads to a model capable of representing the flow at the faces of the actuator surface. Averaging is used to identify the flow at the surface itself.
(3) Fourier analysis is used in Section 2.3 to bring the model to its final form.

2.1. **Potential flow in $\mathbb{R}^3_-$.** The vortex transport equation (6) can be given an equivalent representation with a variation on Euler's equation and a Poisson equation for the attendant pressure field.

$$\frac{\partial \boldsymbol{u}}{\partial t} + \frac{\partial \boldsymbol{u}}{\partial \boldsymbol{x}_e}\boldsymbol{U} = \frac{1}{\rho}\left(\boldsymbol{f} - \nabla_e p\right) \tag{16}$$

$$\nabla_e^2 p = \nabla_e \cdot \boldsymbol{f} \tag{17}$$

Taking the curl of (16) recovers (6) and taking the divergence will result in the Poisson equation (17) for the pressure. The flow in the open lower half-space $\mathbb{R}^3_- := \{\boldsymbol{x}_e : z < 0\}$ will remain irrotational subject to the inequality in (9). Accordingly, the flow in $\mathbb{R}^3_-$ may be represented by a harmonic potential

$$\boldsymbol{u} = \nabla_e \varphi, \quad \nabla_e^2 \varphi = 0, \quad z < 0 \tag{18}$$

Proceeding, (16) may be simplified to the linearized Bernoulli equation shown below.

$$\frac{\partial \varphi}{\partial t} + \frac{\partial \varphi}{\partial \boldsymbol{x}_e}\boldsymbol{U} = -\frac{p}{\rho}, \quad z < 0 \tag{19}$$

The preceding equation holds in the limit $z \uparrow 0$ although not at $z = 0$ itself where the force (8) is nonzero.

A set of fields are now defined on the lower face of the actuator surface.

$$\bar{\varphi}(\boldsymbol{x}, t) := \lim_{z\uparrow 0} \varphi(\boldsymbol{x}_e, t), \quad \bar{p}(\boldsymbol{x}, t) := \lim_{z\uparrow 0} p(\boldsymbol{x}_e, t), \quad \bar{\boldsymbol{u}}(\boldsymbol{x}, t) := \lim_{z\uparrow 0} \boldsymbol{u}(\boldsymbol{x}_e, t) \tag{20}$$

Using the fractional gradient operator developed in Appendix A, Bernoulli's equation (19) can be evaluated in the limit $z \uparrow 0$ where it acquires the form

$$\frac{\partial \bar{\varphi}}{\partial t} + \boldsymbol{U} \cdot \boldsymbol{L}\bar{\varphi} = -\frac{\bar{p}}{\rho}, \quad \bar{\boldsymbol{u}} = \boldsymbol{L}\bar{\varphi} \tag{21}$$

Note that this relation does not depend on the z coordinate, taking only the surface coordinates $\boldsymbol{x}$ and time t as independent variables. The pressure field in (21) is identified by inverting the Poisson equation given in (17). Suppressing the t-argument it holds that

$$p(\boldsymbol{x}_e) = -\int_{\mathbb{R}^3} \frac{\nabla_e' \cdot \boldsymbol{f}(\boldsymbol{x}_e')}{4\pi|\boldsymbol{x}_e - \boldsymbol{x}_e'|}\, d\boldsymbol{x}_e' = -\nabla_e \cdot \int_{\mathbb{R}^3} \frac{\boldsymbol{f}(\boldsymbol{x}_e')}{4\pi|\boldsymbol{x}_e - \boldsymbol{x}_e'|}\, d\boldsymbol{x}_e' = -\nabla_e \cdot \int_{\mathbb{R}^2} \frac{\boldsymbol{F}(\boldsymbol{x}')}{4\pi(|\boldsymbol{x} - \boldsymbol{x}'|^2 + z^2)^{1/2}}\, d\boldsymbol{x}' \tag{22}$$

The second equality is obtained by assuming that $\boldsymbol{f}$ decays at infinity and the third when (8) is inserted and the sifting property of $\delta(z)$ is invoked. Taking the limit as $z \uparrow 0$ leads to the formula

$$\bar{p}(\boldsymbol{x}) = \lim_{z\uparrow 0} p(\boldsymbol{x}_e) = -\frac{\partial}{\partial x_1}\int_{\mathbb{R}^2} \frac{\tau_1(\boldsymbol{x}')}{4\pi|\boldsymbol{x} - \boldsymbol{x}'|}\, d\boldsymbol{x}' - \frac{\partial}{\partial x_2}\int_{\mathbb{R}^2} \frac{\tau_2(\boldsymbol{x}')}{4\pi|\boldsymbol{x} - \boldsymbol{x}'|}\, d\boldsymbol{x}' + \lim_{z\uparrow 0}\int_{\mathbb{R}^2} \frac{z\Delta p(\boldsymbol{x}')}{4\pi(|\boldsymbol{x} - \boldsymbol{x}'|^2 + z^2)^{3/2}}\, d\boldsymbol{x}' \tag{23}$$

The integrand in the last term vanishes outside a small disk centered at $\boldsymbol{x}' = \boldsymbol{x}$ defined by $D_\epsilon := \{\boldsymbol{x} : \ |\boldsymbol{x} - \boldsymbol{x}'| \le \epsilon\}$. This allows the following result

$$\begin{aligned}\lim_{z\uparrow 0}\int_{D_\epsilon} \frac{z\Delta p(\boldsymbol{x}')}{4\pi(|\boldsymbol{x} - \boldsymbol{x}'|^2 + z^2)^{3/2}}\, d\boldsymbol{x}' &= \Delta p(\boldsymbol{x}) \lim_{z\uparrow 0}\int_0^{2\pi}\int_0^{\epsilon} \frac{z}{4\pi(r^2 + z^2)^{3/2}}\, r dr d\theta \\ &= \Delta p(\boldsymbol{x}) \lim_{z\uparrow 0} \frac{1}{2} z\left(\frac{1}{|z|} - \frac{1}{\sqrt{z^2 + \epsilon^2}}\right) = -\frac{1}{2}\Delta p(\boldsymbol{x})\end{aligned} \tag{24}$$

Had the limit been taken from the other side, a result with an opposing sign would ensue. Let an integration kernel be defined by

$$M(\boldsymbol{x}) := \frac{1}{2\pi|\boldsymbol{x}|} \tag{25}$$

Using a convolution operator $(*)$, the pressure distribution appearing in (21) can be given the compact form shown below.

$$\bar{p} = -\frac{1}{2}\left(\frac{\partial(M * \tau_1)}{\partial x_1} + \frac{\partial(M * \tau_2)}{\partial x_2} + \Delta p\right) \tag{26}$$

A model fully specifying the flow at the lower face of the actuator surface is now available in (21) and (26). Notably, the model is expressed in terms of time t and the surface coordinates $\boldsymbol{x}$ with the normal coordinate z being absent.

It is possible to extend the field $\bar{\boldsymbol{u}}$ defined in (20) and modeled by (21) into the lower half-space by noting that the elements of $\boldsymbol{u}$ are harmonic in $\mathbb{R}^3_-$. Absent sources and vorticity one has

$$\nabla_e^2 \boldsymbol{u} = \nabla_e(\nabla_e \cdot \boldsymbol{u}) - \nabla_e \times (\nabla_e \times \boldsymbol{u}) = \boldsymbol{0} \tag{27}$$

This allows the Dirichlet solution (92) found in Appendix A to be utilized. One finds that

$$\boldsymbol{u}(\boldsymbol{x}_e, t) = \int_{\mathbb{R}^2} \frac{-z\bar{\boldsymbol{u}}(\boldsymbol{x}', t)}{2\pi(|\boldsymbol{x} - \boldsymbol{x}'|^2 + z^2)^{3/2}}\, d\boldsymbol{x}', \quad z < 0 \tag{28}$$

2.2. **Jump relations.** The flow undergoes a jump over the actuator surface S at $z = 0$ in the presence of non-zero tangential loading. Let a Gaussian pillbox straddling S be defined by $G := \{\boldsymbol{x}_e : \ |z| \le \epsilon, \ |\boldsymbol{x}| \le \delta\}$ and let the circular base of the pillbox be denoted by the special notation $G_s := \{\boldsymbol{x} : \ |\boldsymbol{x}| \le \delta\}$. The pillbox will be placed at the origin without loss of generality. A jump across S will be symbolized with

$$\Delta f(\boldsymbol{x}) = \lim_{z\downarrow 0} f(\boldsymbol{x}_e) - \lim_{z\uparrow 0} f(\boldsymbol{x}_e) \tag{29}$$

It is assumed that $\partial \boldsymbol{F}/\partial x_i$ and $\partial \boldsymbol{u}/\partial x_i$ are bounded on S for $i = 1, 2$. It is also assumed that $\partial \boldsymbol{u}/\partial t$ is similarly well behaved. Continuity shows that the normal flow perturbation u_n is continuous through S. Letting the thickness of the pillbox tend to zero one finds that

$$\lim_{\epsilon\to 0}\int_G \nabla_e \cdot \boldsymbol{u}\, d\boldsymbol{x}_e = \int_{G_s} \boldsymbol{n} \cdot \Delta \boldsymbol{u}\, d\boldsymbol{x} = 0 \tag{30}$$

Conservation of momentum can be used to identify jumps in the flow components tangential to S. Integrating (16) over the pillbox leads to the relation.

$$\lim_{\epsilon\to 0}\int_G \frac{\partial \boldsymbol{u}}{\partial t} + \frac{\partial \boldsymbol{u}}{\partial \boldsymbol{x}_e}\boldsymbol{U} - \frac{1}{\rho}(\boldsymbol{f} - \nabla_e p)\, d\boldsymbol{x}_e = \int_{G_s} U_n \Delta \boldsymbol{u} - \frac{1}{\rho}(\boldsymbol{F} - \boldsymbol{n}\Delta p)\, d\boldsymbol{x} = \boldsymbol{0} \tag{31}$$

Letting the radius of the pillbox tend to zero so that $\delta \to 0$ identifies the appropriate jump relations as

$$\Delta \boldsymbol{u} = \frac{1}{\rho U_n}\begin{bmatrix} \tau_1 \\ \tau_2 \\ 0 \end{bmatrix} \tag{32}$$

Recalling the definitions in (20), these jumps entail the limits

$$\lim_{z\uparrow 0} \boldsymbol{u} = \bar{\boldsymbol{u}}, \quad \lim_{z\downarrow 0} \boldsymbol{u} = \bar{\boldsymbol{u}} + \Delta \boldsymbol{u} \tag{33}$$

The flow at the surface itself will be described by the special notation

$$\boldsymbol{w} := \boldsymbol{u}|_{z=0}, \quad \boldsymbol{w} := \begin{bmatrix} w_1 \\ w_2 \\ w_n \end{bmatrix} \tag{34}$$

Interpreting $\boldsymbol{w}$ as an average of $\boldsymbol{u}$ over the two sides of S gives rise to the formula

$$\boldsymbol{w} = \frac{\bar{\boldsymbol{u}} + (\bar{\boldsymbol{u}} + \Delta\boldsymbol{u})}{2} = \bar{\boldsymbol{u}} + \frac{1}{2}\Delta\boldsymbol{u} \tag{35}$$

At this stage, the physical basis of the model is complete. The two-dimensional Bernoulli equation (21) can in combination with the pressure model (26) model the flow at the lower face of the actuator disk. Using the representation formula (28) one is able to project this flow into the lower half-space. Finally, the flow at the actuator surface itself as well as its two faces follow from (35) with (32).

2.3. **Fourier analysis.** Fourier analysis is used to bring the formulation to its final form. It is well known that the two dimensional Laplacian operator here symbolized by ∇^2 transforms as

$$\nabla^2 \Leftrightarrow -|\boldsymbol{k}|^2 \tag{36}$$

It turns out that the fractional Laplacian entering through $\boldsymbol{L}$ acquires a very simple interpretation in the frequency domain, namely

$$\sqrt{-\nabla^2} \Leftrightarrow |\boldsymbol{k}| \tag{37}$$

See [Bucur and Valdinoci, 2016] for additional details and generalizations. A transform pair for the fractional operator (99) appearing in (21) can now be identified as

$$\boldsymbol{L} = \begin{bmatrix} \nabla \\ \sqrt{-\nabla^2} \end{bmatrix} \Leftrightarrow \begin{bmatrix} i\boldsymbol{k} \\ |\boldsymbol{k}| \end{bmatrix} = \hat{\boldsymbol{L}} \tag{38}$$

The convolution operator used in the specification of the pressure (26) transforms as

$$M = \frac{1}{2\pi|\boldsymbol{x}|} \Leftrightarrow \frac{1}{|\boldsymbol{k}|} = \hat{M} \tag{39}$$

It it thus seen that $M*$ and $\sqrt{-\nabla^2}$ are mutually inverse operators. This is in agreement with other work involving the fractional Laplacian, see e.g. Gimbutas et al. [2001]. A final result of interest is the Fourier transform pair associated with the kernel in the representation formula (28). This formula can be given in terms of the convolution

$$\boldsymbol{u} = E_z * \bar{\boldsymbol{u}}, \quad E_z(\boldsymbol{x}) := -\frac{z}{2\pi(|\boldsymbol{x}|^2 + z^2)^{3/2}} \tag{40}$$

The appropriate transform pair for E_z is found in Stein and Weiss [1971] but must be modified to comply with the Fourier convention used herein.

$$E_z(\boldsymbol{x}) \Leftrightarrow e^{|\boldsymbol{k}|z}, \quad z < 0 \tag{41}$$

With these transform pairs, the equations governing the flow in $\mathbb{R}^3_-$ may be represented in the Fourier domain.

In $\mathbb{R}^3_-$ the flow derives from a potential. From (21) it follows that the potential and ensuing flow at the lower face of the actuator surface relate as

$$\bar{\boldsymbol{u}} = \boldsymbol{L}\bar{\varphi} \tag{42}$$

Fourier transformation leads to the following formula using (38).

$$\hat{\bar{\boldsymbol{u}}} = \hat{\boldsymbol{L}}\hat{\bar{\varphi}} \tag{43}$$

The normal flow is continuous through the surface as evidenced in (30), therefore the relations

$$\hat{w}_n = |\boldsymbol{k}|\hat{\bar{\varphi}}, \quad \hat{\bar{\boldsymbol{u}}} = |\boldsymbol{k}|^{-1}\hat{\boldsymbol{L}}\hat{w}_n \tag{44}$$

Using (28) and the transform pair (41), the flow in $z < 0$ can be identified in terms of $\hat{w}_n$ as

$$\hat{\boldsymbol{u}} = e^{|\boldsymbol{k}|z}\hat{\bar{\boldsymbol{u}}} = \frac{e^{|\boldsymbol{k}|z}}{|\boldsymbol{k}|}\hat{\boldsymbol{L}}\hat{w}_n, \quad z < 0 \tag{45}$$

The flow at the surface itself is discontinuous. Adding the velocity jump predicted in (32) extends the preceding formula so that it can describe the flow at the actuator surface itself.

$$\hat{\boldsymbol{u}} = \frac{e^{|\boldsymbol{k}|z}}{|\boldsymbol{k}|}\hat{\boldsymbol{L}}\hat{w}_n + \frac{\Theta(z)}{\rho U_n}\begin{bmatrix} \hat{\tau}_1 \\ \hat{\tau}_2 \\ 0 \end{bmatrix}, \quad z \in (-\infty, 0] \tag{46}$$

Heaviside's step function (15) is here used to represent the velocity jump due to the tangential forces. The measurement equation posited at the outset of the section has thus been recovered. One may proceed to find the state equation. Fourier transforming the Bernoulli equation (21) and replacing the potential with the normal flow using (44) leads to

$$\frac{\partial\hat{w}_n}{\partial t} + (\hat{\boldsymbol{L}} \cdot \boldsymbol{U})\hat{w}_n = -\frac{|\boldsymbol{k}|\hat{\bar{p}}}{\rho} \tag{47}$$

From (38) and (39) the surface pressure field described in (26) is seen to Fourier transform as

$$\hat{\hat{p}} = -\frac{\hat{\boldsymbol{L}} \cdot \hat{\boldsymbol{F}}}{2|\boldsymbol{k}|} \tag{48}$$

A state equation is thus obtained on the form shown below.

$$\frac{\partial \hat{w}_n}{\partial t} + (\hat{\boldsymbol{L}} \cdot \boldsymbol{U})\hat{w}_n = \frac{1}{2\rho}(\hat{\boldsymbol{L}} \cdot \hat{\boldsymbol{F}}) \tag{49}$$

Having demonstrated the physical reasoning behind (12) and (14), the discussion proceeds to some selected applications.

3. Unsteady forcing on a disk.

An important problem in the unsteady aerodynamics of wind turbines is the identification of the normal inflow w_n subject to a time-varying application of normal forcing through Δp. Two cases are examined in this section. The first considers the production of vorticity following an impulsive application of force. This example shows that (12) and (14) represents the vortex transport equation (6) correctly. A second example shows how the averaged normal inflow on an actuator disk can be computed exactly in the temporal frequency domain. Using realization theory to extract a time-domain model, the new scheme is put to the test against experiment.

Let polar coordinate systems in Cartesian space and Fourier space be defined respectively by

$$\boldsymbol{x} := \begin{bmatrix} x_1 \\ x_2 \end{bmatrix} = r \begin{bmatrix} \cos(\theta) \\ \sin(\theta) \end{bmatrix}, \quad \boldsymbol{k} := \begin{bmatrix} k_1 \\ k_2 \end{bmatrix} = k \begin{bmatrix} \cos(\vartheta) \\ \sin(\vartheta) \end{bmatrix} \tag{50}$$

Polar descriptions of the forward and inverse Fourier transforms (10) follow as

$$\hat{f}(k,\vartheta) = \int_0^{2\pi}\int_0^{\infty} e^{-ikr\cos(\theta-\vartheta)} f(r,\theta) r \; dr d\theta, \quad f(r,\theta) = \frac{1}{(2\pi)^2}\int_0^{2\pi}\int_0^{\infty} e^{ikr\cos(\theta-\vartheta)} \hat{f}(k,\vartheta) k \; dk d\vartheta \tag{51}$$

3.1. **Impulsive vortex shedding.**

For simplicity, let the pressure jump over a rotor of radius R be applied in the following uniform fashion

$$\Delta p(r,t) = \frac{1}{\pi R^2}\begin{cases} F_0(t) & r \le R \\ 0 & r > R \end{cases} \tag{52}$$

The polar Fourier transform of this field is given by

$$\Delta \hat{p}(k,t) = \frac{2J_1(kR)}{kR} F_0(t) \tag{53}$$

The tangential forces τ_1 and τ_2 are omitted for simplicity. It is assumed that the vorticity generated at the actuator disk convects in an axial manner so that $U_1 = U_2 = 0$. The state equation (12) is thus reduced to the simple relationship

$$\frac{\partial \hat{w}_n}{\partial t}(k,t) + kU_n \hat{w}_n(k,t) = \frac{k}{2\rho}\Delta \hat{p}(k,t) = \frac{2J_1(kR)}{R}\frac{F_0(t)}{2\rho} \tag{54}$$

It will be convenient to examine the dynamics using a Laplace transform. Suppose that U_n is constant in time. Letting s represent the Laplace variable one has

$$\hat{w}_n(k,s) = \frac{1}{s + kU_n}\frac{J_1(kR)}{\rho R} F_0(s) \tag{55}$$

Let $F_0(t)$ acquire the form of an impulse transferring a momentum P to the fluid at $t = t_0$. This is achieved by

$$F_0^\delta(t) = \delta(t - t_0)P \Leftrightarrow F_0^\delta(s) = e^{-t_0 s}P \tag{56}$$

The resulting impulsive flow is described in the Fourier domain with

$$\hat{w}_n^\delta(k,s) = \frac{e^{-t_0 s}}{s + kU_n}\frac{J_1(kR)}{\rho R}P \quad \Rightarrow \hat{w}_n^\delta(k,t) = e^{-kU_n(t-t_0)}\frac{J_1(kR)}{\rho R}\Theta(t - t_0)P \tag{57}$$

Taking an inverse polar Fourier transform results in the following expression

$$\begin{aligned} w_n^\delta(r,t) = \frac{1}{(2\pi)^2}\int_0^{2\pi}\int_0^{\infty} e^{irk\cos(\theta-\vartheta)}\hat{w}^\delta(k,t) k \; dk d\vartheta &= \frac{1}{2\pi}\int_0^{\infty} J_0(kr)\hat{w}^\delta(k,t) k \; dk \\ &= \frac{P\Theta(t-t_0)}{2\pi R\rho}\int_0^{\infty} J_0(kr)J_1(kR)e^{-kU_n(t-t_0)} k \; dk \end{aligned} \tag{58}$$

It is well known that vortex rings are equipped with a momentum equal to $P = \rho\pi R^2 \Gamma$ [Sullivan et al., 2008]. Assuming that the model predicts the creation of a vortex ring also suggests the translation $z(t) = U_n(t - t_0)$ if the ring is convected with the axial transport velocity specified by U_n. In summary, the following flow field is described

$$w_n^\delta(r,t) = \Theta(t - t_0)\frac{\Gamma R}{2}\int_0^{\infty} kJ_0(kr)J_1(kR)e^{-kz(t)} \; dk \tag{59}$$

Consulting Conway [1995], this turns out to be a well known formula that represents a vortex ring of circulation Γ located at the stream-wise coordinate z and of radius R. Heaviside's function serves to "turn the field on" at the moment t_0 where the ring is brought into existence. The state equation (12) is thus seen to model three-dimensional vortex motion using a description set in two dimensions.

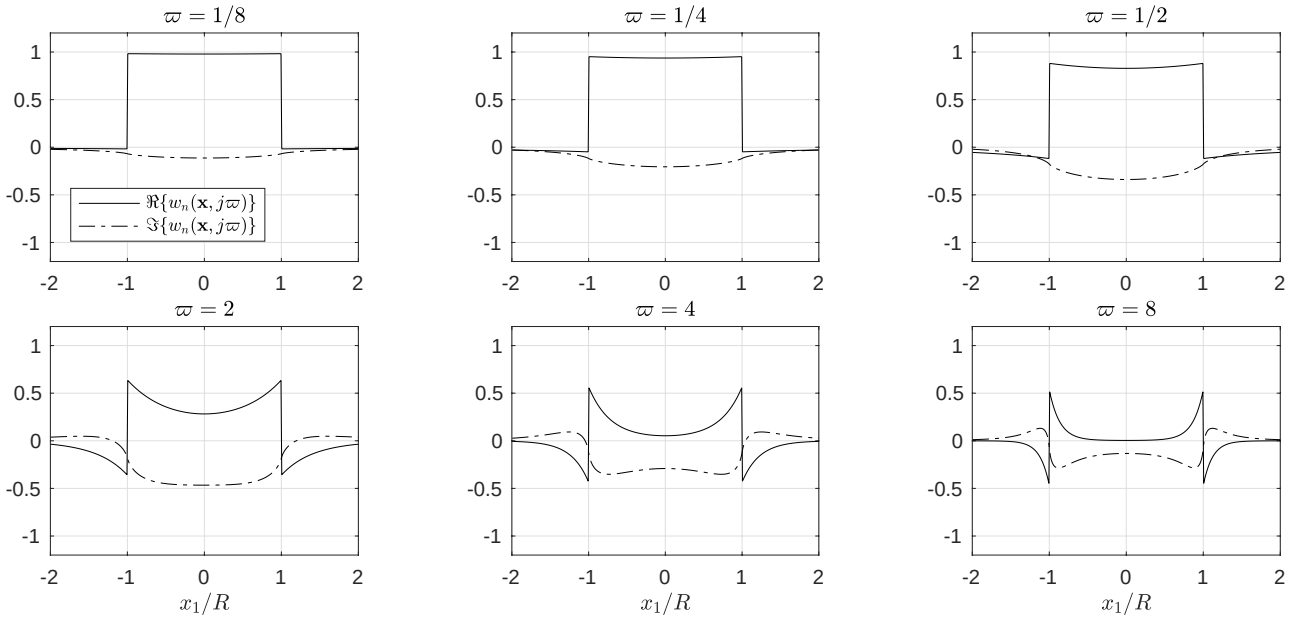

FIGURE 2. The transfer function from quasistatic inflow to dynamic inflow (63) evaluated at the reduced frequency ϖ. Here, the quasistatic inflow is given by $w_n^{\text{qs}}(\tau) = \cos(\varpi\tau)$ and the resulting complex dynamic inflow $w_n(\boldsymbol{x}, j\varpi)$ is shown in a slice running through the centerline at $x_2 = 0$.

3.2. **A transfer function for the inflow.** More elaborate models for vortex production on a uniformly loaded actuator disk can be derived. Generally, $U_n(t)$ will be time-varying. This motivates the introduction of a reduced time τ and a reduced wavenumber κ defined by

$$\frac{\partial \tau}{\partial t} = \frac{U_n}{R}, \quad \kappa = kR \tag{60}$$

With these devices, (54) simplifies to

$$\frac{\partial \hat{w}_n}{\partial \tau}(\kappa, \tau) + \kappa \hat{w}(\kappa, \tau) = 2\pi R^2 J_1(\kappa) w_n^{\text{qs}}(\tau), \quad w_n^{\text{qs}}(\tau) = \frac{F_0(\tau)}{2\rho\pi R^2 U_n(\tau)} \tag{61}$$

The variable w_n^{qs} represents the uniform quasistatic inflow obtained by disregarding dynamics altogether. Let a dimensionless Laplace variable σ be defined by

$$\sigma\tau = st \tag{62}$$

A dimensionless Laplace description of (61) follows as

$$\hat{w}_n(\kappa, \sigma) = \frac{2\pi R^2 J_1(\kappa)}{\sigma + \kappa} w_n^{\text{qs}}(\sigma) \tag{63}$$

This equation is quite interesting since it showcases the non-locality arising from the fractional dynamics of (12). Let the reduced Laplace variable expand as $\sigma = \varrho + j\varpi$. Evaluating (63) along the imaginary axis produces the frequency response shown in Figure 2. The quasistatic inflow is uniform over the disk and vanishes elsewhere. However, the dynamic inflow exhibits significant entrainment of the flow outside the disk. Note also the significant distortion and phase shift associated with harmonic excitation.

It is also possible to extract the averaged inflow over the actuator disk. This can be done through Parseval's formula [Hörmander, 2003]. In Cartesian coordinates one has

$$\int_{\mathbb{R}^2} f(\boldsymbol{x}) g^*(\boldsymbol{x}) \, d\boldsymbol{x} = \frac{1}{(2\pi)^2} \int_{\mathbb{R}^2} \hat{f}(\boldsymbol{k}) \hat{g}^*(\boldsymbol{k}) \, d\boldsymbol{k} \tag{64}$$

Conversion to a polar description allows this formula to be applied in the following manner

$$w_n^{\text{av}}(\sigma) := \frac{1}{\pi R^2} \int_0^{2\pi} \int_0^R w_n(r, \sigma) r \, dr d\theta = \frac{1}{\pi R^2} \frac{1}{2\pi} \int_0^{2\pi} \int_0^\infty J_1(\kappa) \hat{w}_n(\kappa, \sigma) \, d\kappa d\vartheta = \left[\int_0^\infty \frac{2J_1^2(\kappa)}{\sigma + \kappa} \, d\kappa \right] w_n^{\text{qs}}(\sigma) \tag{65}$$

The dimensionless transfer function relating $w_n^{\text{qs}}(\sigma)$ to the averaged flow $w_n^{\text{av}}(\sigma)$ will be denoted by

$$\mathcal{Q}(\sigma) := \frac{w_n^{\text{av}}}{w_n^{\text{qs}}}(\sigma) = \int_0^\infty \frac{2J_1^2(\kappa)}{\sigma + \kappa} \, d\kappa \tag{66}$$

An amplitude-phase diagram of (66) is shown in Figure 3. Note the low-pass behavior with decreasing gain at high frequency excitation. This implies that the effective inflow will be smaller than the quasistatic prediction under time-varying loading. The DC-gain of the transfer function is unity implying an equilibrium defined by

$$w_n^{\text{av}} = w_n^{\text{qs}} = \frac{F_0}{2\rho\pi R^2 U_n} \tag{67}$$

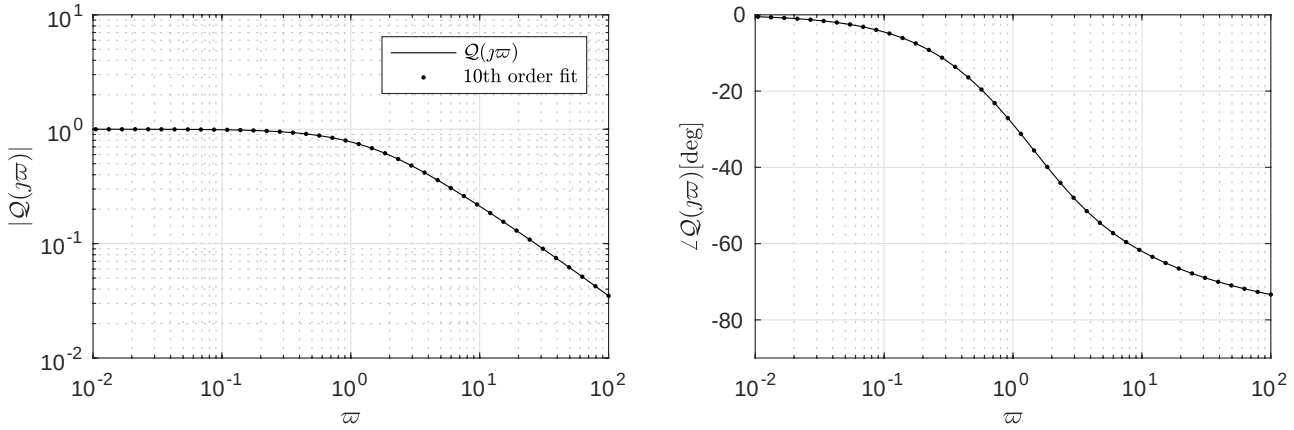

FIGURE 3. Bode diagram of (66) and a finite-dimensional fit (69).

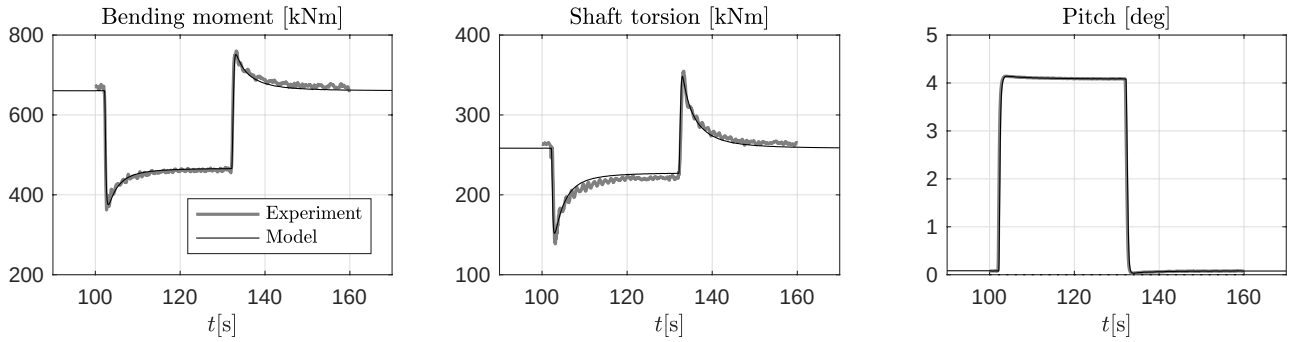

FIGURE 4. The transfer function (66) used with a BEMT code, compared to experiment.

Letting $U_0(t)$ represent a uniform wind speed and choosing the normal transport velocity as done below recovers Rankine-Froude momentum theory at steady state.

$$U_n(t) = U_0(t) + w_n^{\mathrm{av}}(t) \tag{68}$$

It must thus be assumed that vorticity travels downstream at a speed equal to the averaged flux through the actuator disk.

Realization. The filter (66) is distributed and cannot be represented exactly by a finite number of states. However, realization theory [Chen, 2014] can be used to generate a finite dimensional estimate. A lumped transfer-function and associated state-space model given in dimensionless time are shown below.

$$\mathcal{Q}(\sigma) \simeq \boldsymbol{c}(\sigma\boldsymbol{I} - \boldsymbol{A})^{-1}\boldsymbol{b}, \quad \frac{\partial \boldsymbol{z}}{\partial \tau}(\tau) = \boldsymbol{A}\boldsymbol{z}(\tau) + \boldsymbol{b}w_n^{\mathrm{qs}}(\tau), \quad w_n^{\mathrm{av}}(\tau) = \boldsymbol{c}\boldsymbol{z}(\tau) \tag{69}$$

The fit achieved by a 10th order system using the methodology described in Gustavsen and Semlyen [1999] is indicated in Figure 3. Reversion to dimensional time is achieved using (60) to replace the derivative with respect to τ. Inserting the definition of w_n^{qs} found in (61) leads to the approximate time-domain model shown below.

$$R\frac{\partial \boldsymbol{z}}{\partial t}(t) = U_n(t)\boldsymbol{A}\boldsymbol{z}(\tau) + \boldsymbol{b}\frac{F_0(t)}{2\rho\pi R^2}, \quad w_n^{\mathrm{av}}(t) = \boldsymbol{c}\boldsymbol{z}(t) \tag{70}$$

Replacing the quasistatic inflow in a basic blade-element momentum theory (BEMT) code with the dynamic inflow predicted by the time domain-model (70) allows an assessment of the underlying theory. The time-series data described in [Øye, 1991] taken at the Tjæreborg turbine are used for comparison. This data describes the mean flap moment $M_{\mathrm{flap}}(t)$, low-speed shaft torque $Q(t)$ and generator shaft power $E(t)$ as the pitch $\beta(t)$ undergoes step changes. The experimenters used averaging to remove noise from 1P and 3P variations as well as variations in the wind speed. The data used herein therefore represents the mean over $n = 58$ identical experiments. Minor adjustments (on the order of a few percent) were made to the numerical parameters in the blade-element model so that the bias values matched well. The only tuning on (70) was a tip-loss correction to the radius R using an effective radius $R' = 0.95R$. This idea was based on the simplified tip-loss model in Johnson [1994]. The graphs shown in Figure 4 indicate that the transients predicted by (66) capture the true physics with high fidelity.

3.3. **Previous work.** It is interesting to compare the present model with existing work in the field. Two main approaches seem to dominate the science, methods based on the acceleration potential and vortex methods. Examples from both approaches are discussed below.

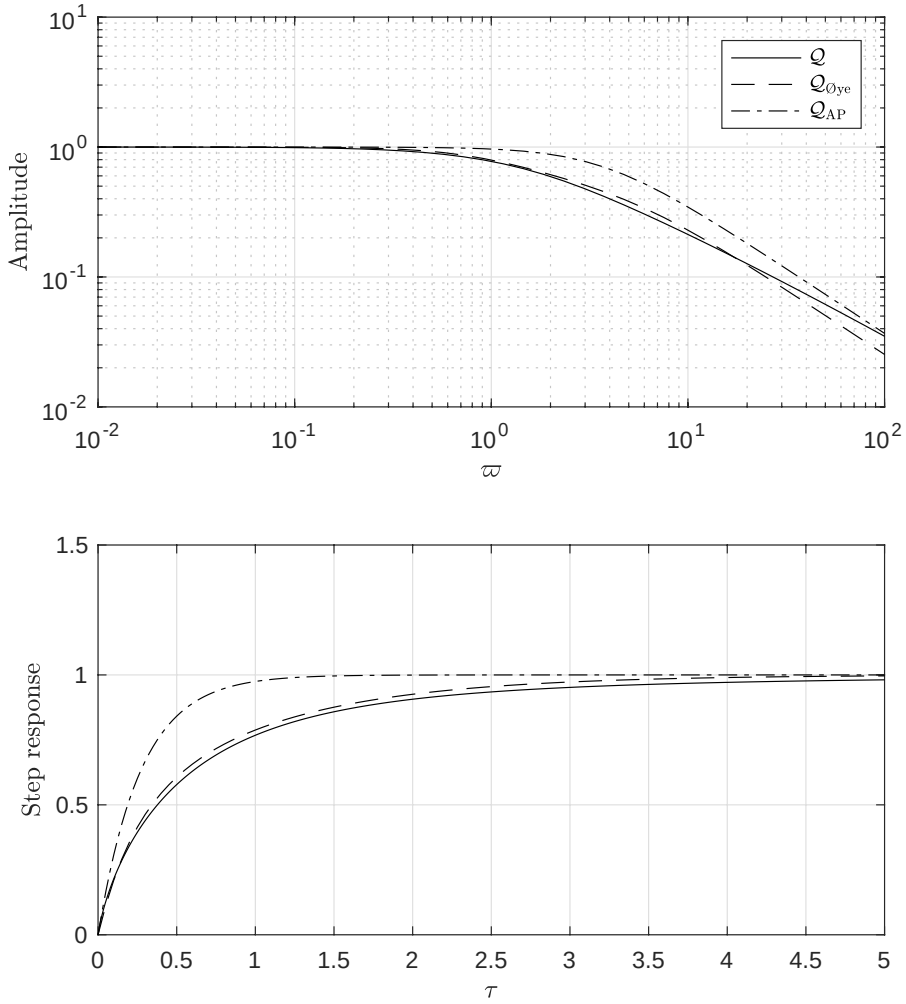

FIGURE 5. Above: Amplitude of the frequency response for the filters (66), (77) and (82). Below: Step response of the averaged inflow $w_n^{\text{av}}(\tau)$ in reduced time with the input $w_n^{\text{qs}}(\tau) = \Theta(\tau)$.

Øye's vortex model. The dynamic inflow model developed in this work is not unique in being informed by vortex theory. A notable example is the pragmatic time-domain model proposed in Øye [1986]. See also [Hansen, 2008]. In this model, a second order nonlinear filter is employed to generate a transient response which correlates well to experimental data. Øye's model is supplied on the form of a nonlinear filter cascade taking a quasistatic inflow w_n^{qs} into a dynamic inflow $w_n(r,t)$.

$$T_1(t)\dot{w}_1(t) + w_1(t) = kT_1(t)\dot{w}_n^{\text{qs}}(t) + w_n^{\text{qs}}(t) \tag{71a}$$

$$T_2(r,t)\dot{w}_n(r,t) + w_n(r,t) = w_1(t) \tag{71b}$$

The time-varying coefficients in the filter are given by

$$T_1(t) = \frac{1.1}{1-1.3a(t)}\frac{R}{U_0(t)}, \quad T_2(r,t) = (0.39 - 0.26(r/R)^2)T_1(t), \quad k = 0.6 \tag{72}$$

Here, U_0 denotes the free-stream velocity and a the inflow factor. The inflow factor will be approximated by the average $a \simeq -w_n^{\text{av}}/U_0$ in the following. Furthermore, the form of (71) will be altered slightly to allow comparison with the present model.

Assuming moderate inflow $a < 1/3$ and invoking (68) permits the approximation

$$T_1 \approx \frac{R}{U_n} \tag{73}$$

Using (60) and changing variables from t to the dimensionless time τ linearizes the filter cascade

$$\frac{dw_1}{d\tau}(\tau) + w_1(\tau) = k\frac{dw_i^{\text{qs}}}{d\tau}(\tau) + w_i^{\text{qs}}(\tau) \tag{74a}$$

$$(0.39 - 0.26(r/R)^2)\frac{dw_n}{d\tau}(r,\tau) + w_n(r,\tau) = w_1(\tau) \tag{74b}$$

The Laplace transform of this system can be used to obtain the following relation

$$w_n(r,\sigma) = \frac{1}{(0.39 - 0.26(r/R)^2)\sigma + 1}\frac{k\sigma+1}{\sigma+1}w_n^{\text{qs}}(\sigma) \tag{75}$$

One may proceed to extract the averaged inflow in the following manner

$$w_n^{\mathrm{av}}(\sigma) = \left[\frac{1}{\pi R^2}\int_0^R \frac{2\pi r}{(0.39-0.26(r/R)^2)\sigma+1}\,dr\right]\frac{k\sigma+1}{\sigma+1}w_n^{\mathrm{qs}}(\sigma) \tag{76}$$

A transfer function analogous to (66) is thus obtained as

$$\mathcal{Q}_{\mathrm{\O ye}}(\sigma) = \frac{(0.6\sigma+1)(3.85\log(\sigma+2.56)-3.85\log(\sigma+7.69)+4.23)}{\sigma(\sigma+1)} \tag{77}$$

The frequency response of this function is shown in Figure 5 where it can be compared to the result obtained using the new theory. The two transfer functions and their step responses are indeed very similar.

Acceleration potential models. Inflow models exemplified by a mass-damper system seems to have originated with the work of Carpenter and Fridovich [1953] where the effects of rapid blade pitching on a helicopter was examined. Their model is given below.

$$m_a\dot{w}_n^{\mathrm{av}} + 2\rho\pi R^2 U_n w_n^{\mathrm{av}} = F_0 \tag{78}$$

The damping term is simply that furnished by Rankine-Froude momentum theory [Froude, 1889]. The novelty in [Carpenter and Fridovich, 1953] was the addition of an apparent mass term m_a which represents the lag in inflow following a change in thrust. This "mass" was suggested to be 63.7% of a sphere of fluid with radius equal to the rotor. To close approximation, one may write

$$m_a = \frac{8}{3\pi}\rho\pi R^3 \tag{79}$$

The basic mass-damper model was refined by Pitt and Peters [Pitt and Peters, 1981] who, in addition to modeling the effects of forward flight, arrived at the same value for the apparent mass. The mass was corrected in later works to the following value [Peters and HaQuang, 1988]

$$m_a = \frac{128}{75\pi}\rho\pi R^3 \tag{80}$$

This family of models are similar to the acceleration-potential method of van Bussel [Van Bussel, 1995] in that they both employ a methodology originating with Kinner [1936]. This approach solves a Laplace equation for the pressure in an oblate spheroidal coordinate system permitting separation of variables. The resulting solution (given as a harmonic expansion) is related to the flow field under an assumption of small perturbation flow. Methods of this general class [Burton et al., 2001, Van Bussel, 1995] all seem to suggest the added mass (80). The mathematics underlying the acceleration-potential method are rather involved, consult [Peters et al., 1989, Van Bussel, 1995] for details.

Expressing (78) in reduced time and using the quasistatic inflow in (61) leads to the following formulation

$$\frac{m_a}{2\rho\pi R^3}\frac{\partial w_n^{\mathrm{av}}}{\partial\tau} + w_n^{\mathrm{av}} = w_n^{\mathrm{qs}} \tag{81}$$

Using the virtual mass from (80) and Laplace transforming the preceding ODE yields yet another analogue of (66) useful for comparison purposes.

$$\mathcal{Q}_{\mathrm{AP}}(\sigma) = \frac{1}{\frac{64}{75\pi}\sigma+1} \tag{82}$$

This transfer-function is a simple first-order low-pass filter.

Comparison. As shown in Figure 5 the filters obtained using the present approach and Øye theory correspond very well, both in the frequency and time domains. Both filters are well suited for wind turbine modeling, as evidenced in Figure 4. The acceleration potential deviates significantly and exhibits much faster transients. Acceleration potential methods have been extended to permit computation of disk-varying inflow generated by a pressure distribution that is allowed to vary over the actuator disk. Peters et al. [1989] underscores that these generalized variations contain the simple scalar model exemplified by (78) and (80) as a special case. This implies that the disagreement indicated in Figure 5 should persist even if more advanced versions of the acceleration-potential method is used.

4. Yawed operation

An important application of vortex theory has been to examine the inflow under yawed conditions. The vortex transport velocity can be chosen to model this case by letting χ represent the yaw angle and setting

$$\boldsymbol{U} = |\boldsymbol{U}|\begin{bmatrix}\sin(\chi)\\0\\\cos(\chi)\end{bmatrix}, \quad -\frac{\pi}{2}<\chi<\frac{\pi}{2} \tag{83}$$

The bound on the skew angle is necessary to satisfy the inequality (9) on the normal transport velocity. Neglecting tangential loading and assuming steady operation reduces (12) to

$$\hat{w}_n(k,\vartheta) = \frac{1}{\cos(\chi)+i\sin(\chi)\cos(\vartheta)}\frac{\Delta\hat{p}(k,\vartheta)}{2\rho|\boldsymbol{U}|} \tag{84}$$

The polar coordinates defined in (50) have been used to simplify the expression. The main problem with this relation is the inverse Fourier transform needed to arrive at $w_n(r,\theta)$. As evidenced in Coleman et al. [1945] and Branlard and Gaunaa [2016] quite daunting integrals must be tackled using conventional vortex theory. Their challenges with the Biot-Savart law are here replaced with the inverse transform.

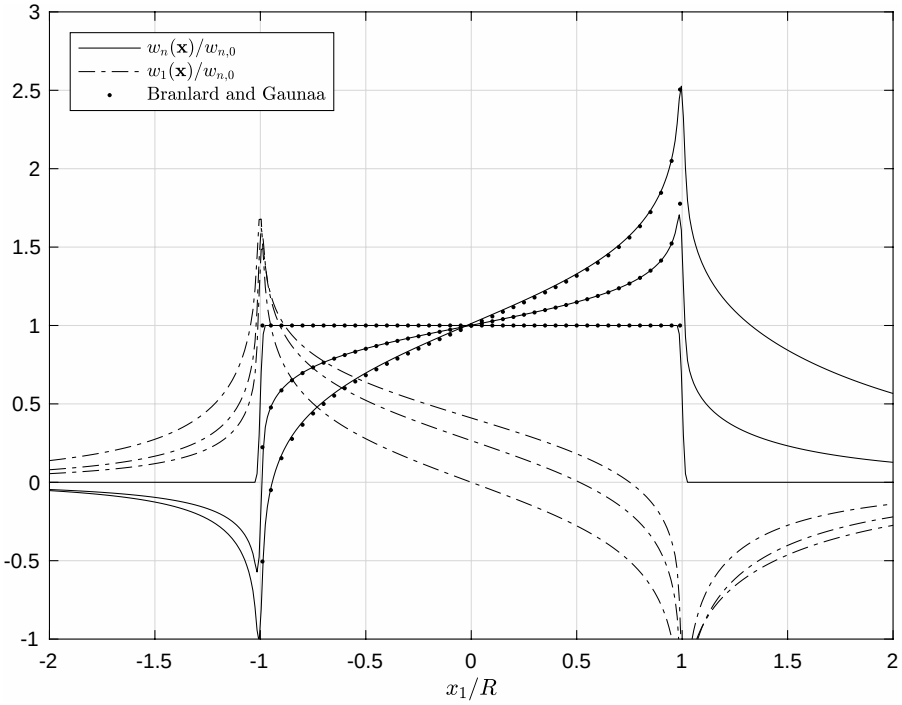

FIGURE 6. Normalized inflow at $z = x_2 = 0$ at inflow angles $\chi = 0°$, $30°$ and $60°$. The inflow component w_2 is identically zero at the centerline.

Assume for simplicity that the pressure jump satisfies $\Delta\hat{p} = \Delta\hat{p}(k)$. Now,

$$w_n(r,\theta) = \frac{1}{2\pi}\int_0^\infty \left(\frac{1}{2\pi}\int_0^{2\pi} \frac{e^{irk\cos(\theta-\vartheta)}}{\cos(\chi)+i\sin(\chi)\cos(\vartheta)}d\vartheta\right)\frac{k\Delta\hat{p}(k)}{2\rho|\boldsymbol{U}|}\,dk \tag{85}$$

Evaluation at the centerline $\theta = \pi/2 \mp \pi/2$ and linearization in $t = \tan(\chi/2)$ permits the estimate

$$w_n(r,\pi/2\mp\pi/2) \simeq \frac{1}{2\rho|\boldsymbol{U}|}\frac{1}{2\pi}\int_0^\infty (J_0(kr) \pm 2\tan(\chi/2)J_1(kr))\Delta\hat{p}(k)k\,dk \tag{86}$$

Let $k' := kR$. Inserting the uniform loading in (53) and evaluating the transform, one arrives at the following estimate valid in the interval $r \in [0, R)$.

$$\begin{aligned} w_n(r,\theta) &\simeq \frac{F_0}{2\pi R^2\rho|\boldsymbol{U}|}\int_0^\infty J_1(k')(J_0(k'r/R)+2\cos(\theta)\tan(\chi/2)J_1(k'r/R))dk \\ &= \frac{F_0}{2\pi R^2\rho|\boldsymbol{U}|}\left[1+\frac{r}{R}\cos(\theta)\tan\left(\frac{\chi}{2}\right)\frac{4(K[(r/R)^2]-E[(r/R)^2])}{\pi(r/R)^2}\right] \end{aligned} \tag{87}$$

The special notation K and E represent complete elliptic integrals of the first and second kind, respectively. Let the following notation apply

$$w_{n,0} := \frac{F_0}{2\pi R^2\rho|\boldsymbol{U}|}, \quad \mathcal{K}(\mu,\chi) := \tan\left(\frac{\chi}{2}\right)\frac{4(K[\mu^2]-E[\mu^2])}{\pi\mu^2} \tag{88}$$

An expression in the scheme of Glauert theory can thus be extracted as

$$w_n(r,\theta) = w_{n,0}\left[1+\frac{r}{R}\cos(\theta)\mathcal{K}\left(\frac{r}{R},\chi\right)\right] \tag{89}$$

This result corresponds to the flow expansion $F(\mu)$ found in Burton et al. [2001] via the identity $\mu\mathcal{K}(\mu,\chi) = 2F(\mu)\tan(\chi/2)$. The integral in [Burton et al., 2001, eq. 3.116] (which contains a typographical error) is thus given an explicit form.

Bypassing the analytical integration with the spectral method in Appendix B allows additional predictions. Inflow at the centerline $x_2 = 0$ are shown in Figure 6. Exacts result from the vortex theory described in Branlard and Gaunaa [2016] are compared to the predictions from the model developed in this work. The numerical algorithm detailed in Appendix B is seen to acquit itself well. It is noted that other results from Branlard and Gaunaa [2016] and earlier works such as Coleman et al. [1945] may be reproduced as well. An illustration not confined to the centerline is shown in Figure 7.

4.1. **Harmonic excitation.** A distinguishing capability of the new model is the ability to represent the effects of unsteady loading with high fidelity. It has been demonstrated that the model captures dynamics well in Section 3. Furthermore, predictions with a skewed wake correspond to well known results. Combining these capabilities gives a tool that can compute dynamic inflow with significant yaw misalignment.

Consider the simulation shown in Figure 8. Here, the inflow distribution due to a sinusoidal force applied uniformly on an actuator disk in skewed flow is shown. Interestingly, it is possible to distinguish the persistent effects of past loading,

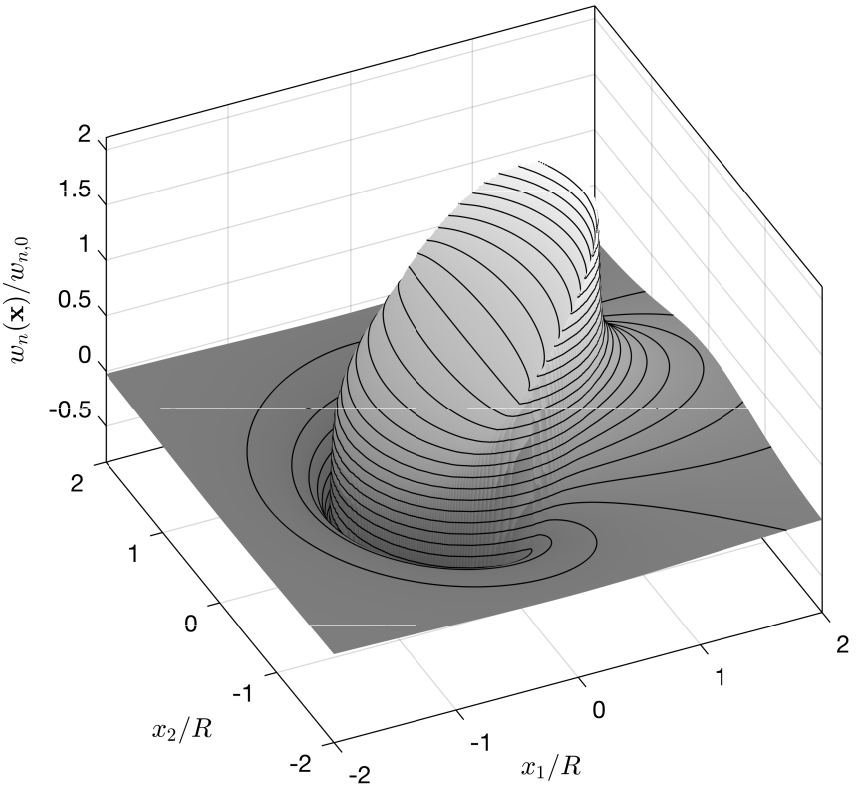

FIGURE 7. Normalized inflow at $z = 0$ with an inflow angle $\chi = 45°$ computed numerically. The contours indicate isolines of w.

although the diffusive nature of the dynamics leads to quick dissipation of these traces. A three-dimensional vortex tube appears in the simulation, even though the new theory is set in two dimensions. This can be understood by interpreting the fractional state equation (12) as a "holographic" representation of the three-dimensional vortex transport equation (6).

The efficiency of the Fast Fourier Transform (FFT) enables fine-grained numerical simulations such as the one shown in Figure 8. A rectangular domain of dimensions $20R \times 20R$ with R being the rotor radius was used for computation, so only a small portion of the result is shown. Some numerical artifacts, arising when a rectangular grid is used to represent a circular object, are visible as fringes on the disk's circumference.

5. Conclusion

This work has introduced a new approach for inflow predictions on an actuator disk. The resulting Actuator Disc Vortex Theory has been compared favorably to experimental data and existing exact solutions. Interestingly, this has been achieved with a theoretical framework departing quite significantly from previous approaches. The new method is useful for three main reasons.

(1) Steady and unsteady vortex theory are unified seamlessly without undue loss of analytical precision.
(2) The method encompasses a wide range of applications due to its general formulation in (12) and (14).
(3) The formulation is simple and compact.

The experimental study depicted in Figure 4 shows that the proposed fractional dynamics are physically meaningful. This should serve as justification for the somewhat exotic mathematics.

There are also certain drawbacks to the method. Numerical evaluation is necessary in most practical situations and an effective discretization scheme such as the one employed by the GDW model is not yet available. The spectral method detailed in Appendix B is very efficient since it can utilize the Fast Fourier transform. However, the rectangular grid creates problems with sampling circular objects and requires a fairly high resolution for smooth results. The periodic boundary conditions associated with the discrete Fourier Transform (DFT) requires a large computational domain since the object of study must be well removed from the boundaries. In axial flow, this is not a problem due to the diffusive nature of the physics. However, skew angles approaching 90° cannot be modeled since shed vortices will return periodically.

It should be noted that this work has only scratched the surface of the model's capabilities. The presentation given above is mainly aimed at establishing the physical soundness of the method based on some simple examples. Further

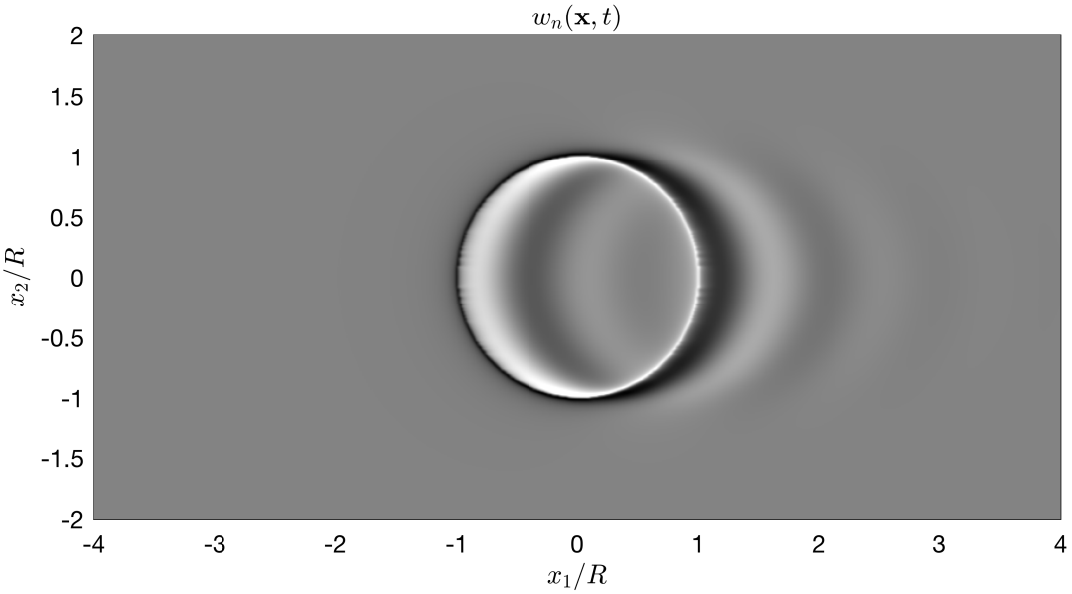

FIGURE 8. Inflow at $z = 0$ under sinusoidal load application with an inflow angle $\chi = 75°$, computed numerically. Lighter shades indicate higher inflow values. A vortex tube extending down and to the right can be gleaned.

work should be undertaken on more refined numerical schemes and efficient discretization methods for engineering applications.

Appendix A. A Fractional Gradient Operator

A definition of the fractional Laplacian in two dimensions and with exponent $s = 1/2$ can be found in Bucur and Valdinoci [2016].

$$\sqrt{-\nabla^2} g(\boldsymbol{x}) = \text{p.v.} \int_{\mathbb{R}^2} \frac{g(\boldsymbol{x}) - g(\boldsymbol{x}')}{2\pi|\boldsymbol{x} - \boldsymbol{x}'|^3} \, d\boldsymbol{x}' \tag{90}$$

Let $h(\boldsymbol{x}_e)$ be harmonic in the lower half-space $\mathbb{R}^3_-$ and satisfy a Dirichlet boundary condition on $z = 0$.

$$\nabla_e^2 h(\boldsymbol{x}_e) = 0, \quad z < 0, \quad \lim_{z \uparrow 0} h(\boldsymbol{x}_e) = H(\boldsymbol{x}) \tag{91}$$

An expression for $\nabla_e h$ on $z = 0$ in terms of H is sought. This is accomplished by a dimensional reduction involving the fractional Laplacian defined above. Butzer [1961] provides a solution to the Dirichlet problem (91) in terms of the representation shown below.

$$h(\boldsymbol{x}_e) = \int_{\mathbb{R}^2} \frac{-zH(\boldsymbol{x}')}{2\pi(|\boldsymbol{x} - \boldsymbol{x}'|^2 + z^2)^{3/2}} \, d\boldsymbol{x}', \quad z < 0 \tag{92}$$

Differentiating (92) with respect to the normal coordinate z leads to the formula

$$\frac{\partial h}{\partial z}(\boldsymbol{x}_e) = \int_{\mathbb{R}^2} \frac{-H(\boldsymbol{x}')}{2\pi(|\boldsymbol{x} - \boldsymbol{x}'|^2 + z^2)^{3/2}} \, d\boldsymbol{x}' + \int_{\mathbb{R}^2} \frac{3z^2 H(\boldsymbol{x}')}{2\pi(|\boldsymbol{x} - \boldsymbol{x}'|^2 + z^2)^{5/2}} \, d\boldsymbol{x}' \tag{93}$$

The derivative is now evaluated in the limit $z \uparrow 0$. This is a delicate operation due to the singular integrals. Let a small disk with a radius ϵ tending to zero be defined by

$$D_\epsilon := \{\boldsymbol{x}' : |\boldsymbol{x} - \boldsymbol{x}'| \leq \epsilon\} \tag{94}$$

The integrals in (93) are evaluated in two pieces; a regular part over $\mathbb{R}^2 \backslash D_\epsilon$ and a singular part over D_ϵ. The regular part gives rise to the principal value integral derived below

$$\lim_{z \uparrow 0} \left[\int_{\mathbb{R}^2 \backslash D_\epsilon} \frac{-H(\boldsymbol{x}')}{2\pi(|\boldsymbol{x} - \boldsymbol{x}'|^2 + z^2)^{3/2}} \, d\boldsymbol{x}' + \int_{\mathbb{R}^2 \backslash D_\epsilon} \frac{3z^2 H(\boldsymbol{x}')}{2\pi(|\boldsymbol{x} - \boldsymbol{x}'|^2 + z^2)^{5/2}} \, d\boldsymbol{x}' \right] = - \int_{\mathbb{R}^2 \backslash D_\epsilon} \frac{H(\boldsymbol{x}')}{2\pi|\boldsymbol{x} - \boldsymbol{x}'|^3} \, d\boldsymbol{x}' \tag{95}$$

Assuming that H is sufficiently well behaved to be considered constant within the small disk permits the following procedure for the singular part

$$\begin{aligned} \lim_{z \uparrow 0} \left[\int_{D_\epsilon} \frac{-H(\boldsymbol{x}')}{2\pi(|\boldsymbol{x} - \boldsymbol{x}'|^2 + z^2)^{3/2}} \, d\boldsymbol{x}' + \int_{D_\epsilon} \frac{3z^2 H(\boldsymbol{x}')}{2\pi(|\boldsymbol{x} - \boldsymbol{x}'|^2 + z^2)^{5/2}} \, d\boldsymbol{x}' \right] \\ = H(\boldsymbol{x}) \lim_{z \uparrow 0} \int_0^{2\pi} \int_0^{\epsilon} \frac{2z^2 - r^2}{2\pi(r^2 + z^2)^{5/2}} \, r dr d\theta = H(\boldsymbol{x}) \lim_{z \uparrow 0} \frac{\epsilon^2}{(\epsilon^2 + z^2)^{3/2}} = \frac{1}{\epsilon} H(\boldsymbol{x}) \end{aligned} \tag{96}$$

This result may be compared to the integral

$$\int_{\mathbb{R}^2\setminus D_\epsilon} \frac{1}{2\pi|\boldsymbol{x}-\boldsymbol{x}'|^3}\, d\boldsymbol{x}' = \int_0^{2\pi}\int_\epsilon^\infty \frac{1}{2\pi r^3}\, r dr d\theta = \frac{1}{\epsilon} \tag{97}$$

Gathering results and taking the limit $\epsilon \to 0$ provides the normal derivative in the form of a principal value integral representing the fractional Laplacian.

$$\lim_{z\uparrow 0} \frac{\partial h}{\partial z}(\boldsymbol{x}_e) = \text{p.v.} \int_{\mathbb{R}^2} \frac{H(\boldsymbol{x})-H(\boldsymbol{x}')}{2\pi|\boldsymbol{x}-\boldsymbol{x}'|^3}\, d\boldsymbol{x}' = \sqrt{-\nabla^2} H(\boldsymbol{x}) \tag{98}$$

Let the fractional gradient operator be defined by

$$\boldsymbol{L} := \begin{bmatrix} \nabla \\ \sqrt{-\nabla^2} \end{bmatrix}, \quad \nabla = \begin{bmatrix} \frac{\partial}{\partial x_1} \\ \frac{\partial}{\partial x_2} \end{bmatrix} \tag{99}$$

Using the fractional gradient operator $\boldsymbol{L}$ one can represent the three-dimensional gradient at the surface $z = 0$ using operations involving only the surface coordinates $\boldsymbol{x}$. A dimensional reduction has thus been effected.

$$\lim_{z\uparrow 0} \nabla_e h = \boldsymbol{L} H \tag{100}$$

Appendix B. Numerical solution

A spectral method on a rectangular grid of dimensions $X_1 \times X_2$ and resolution $N_1 \times N_2$ (even N_i assumed) is utilized for numerical work. DFT is used for spatial discretization and periodic boundary conditions are imposed for simplicity.

By way of example, let $f(x_1, x_2)$ denote a continuous field on $\mathbb{R}^2$. A sampled field is obtained from

$$f_s[n_1, n_2] = f\left(\frac{X_1}{N_1} n_1, \frac{X_2}{N_2} n_2\right), \quad n_i = 0 \ldots N_i - 1 \tag{101}$$

The spectral method is based on the discrete Fourier transform whose forward and reverse transforms are defined by

$$\hat{f}_s[l_1, l_2] = \sum_{n_1=0}^{N_1-1} \sum_{n_2=0}^{N_2-1} f_s[n_1, n_2] e^{-2\pi i\left(\frac{n_1}{N_1} l_1 + \frac{n_2}{N_2} l_2\right)} \tag{102a}$$

$$f_s[n_1, n_2] = \frac{1}{N_1 N_2} \sum_{l_1=0}^{N_1-1} \sum_{l_2=0}^{N_2-1} \hat{f}_s[l_1, l_2] e^{2\pi i\left(\frac{n_1}{N_1} l_1 + \frac{n_2}{N_2} l_2\right)} \tag{102b}$$

A band-limited DFT-based interpolant for the field $f(x_1, x_2)$ will be used. Let A be an even integer and let a function be given as

$$b_A[a] = \begin{cases} a & a \le A/2 \\ a - A & a > A/2 \end{cases} \qquad A \text{ even} \tag{103}$$

This device converts frequencies above the Nyquist limit $A/2$ into their negative and band-limited aliases. Now, $f(x_1, x_2)$ can be given the DFT-based interpolation shown below

$$f_p(x_1, x_2) = \frac{1}{N_1 N_2} \sum_{l_1=0}^{N_1-1} \sum_{l_2=0}^{N_2-1} \hat{f}_s[l_1, l_2] e^{2\pi i\left(\frac{x_1}{X_1} b_{N_1}[l_1] + \frac{x_2}{X_2} b_{N_2}[l_2]\right)} \tag{104}$$

The continuous Fourier transform $\hat{f}_p(k_1, k_2)$ of the interpolant is concentrated at discrete frequencies given by

$$k_1 = 2\pi \frac{b_{N_1}[l_1]}{X_1}, \quad k_2 = 2\pi \frac{b_{N_2}[l_2]}{X_2} \tag{105}$$

Frequency decoupling permits the following discretization of the state equation (12) where elements in the DFT transform of the sampled fields $\hat{w}_{n,s}[l_1, l_2, t]$ and $\hat{\boldsymbol{F}}_s[l_1, l_2, t]$ can be considered on an element by element basis.

$$\frac{\partial \hat{w}_{n,s}}{\partial t} + (\hat{\boldsymbol{L}}_s \cdot \boldsymbol{U}) \hat{w}_{n,s} = \frac{1}{2\rho} (\hat{\boldsymbol{L}}_s \cdot \hat{\boldsymbol{F}}_s) \tag{106}$$

The measurement equation discretizes in a similar fashion.

$$\hat{\boldsymbol{u}}_s = \frac{e^{|\boldsymbol{k}_s| z}}{|\boldsymbol{k}_s|} \hat{\boldsymbol{L}}_s \hat{w}_{n,s} + \frac{\Theta(z)}{\rho U_n} \begin{bmatrix} \hat{F}_{1,s} \\ \hat{F}_{2,s} \\ 0 \end{bmatrix} \tag{107}$$

Here, the discrete operators associated with the frequencies $l_i = 0 \ldots N_i - 1$ read as

$$\boldsymbol{k}_s = 2\pi \begin{bmatrix} b_{N_1}[l_1]/X_1 \\ b_{N_2}[l_2]/X_2 \end{bmatrix}, \quad \hat{\boldsymbol{L}}_s = \begin{bmatrix} i\boldsymbol{k}_s \\ |\boldsymbol{k}_s| \end{bmatrix} \tag{108}$$

One may proceed to use the discretized formulae (106) and (107) in much the same manner as the original expressions in (12) and (14).

References

E. Branlard and M. Gaunaa. Cylindrical vortex wake model: right cylinder. *Wind Energy*, 18(11):1973–1987, 2015.

E. Branlard and M. Gaunaa. Cylindrical vortex wake model: skewed cylinder, application to yawed or tilted rotors. *Wind Energy*, 19(2):345–358, 2016.

C. Bucur and E. Valdinoci. *Nonlocal diffusion and applications*, volume 20 of *Lecture Notes of the Unione Matematica Italiana*. Springer, 2016.

T. Burton, D. Sharpe, N. Jenkins, and E. Bossanyi. *Wind Energy Handbook*. John Wiley & Sons Ltd., Chichester, West Sussex, 2001.

P. Butzer. On dirichlet's problem for the half-space and the behavior of its solution on the boundary. *Journal of Mathematical Analysis and Applications*, 2(1):86–96, 1961.

L. A. Caffarelli and A. Vasseur. Drift diffusion equations with fractional diffusion and the quasi-geostrophic equation. *Annals of Mathematics*, pages 1903–1930, 2010.

P. J. Carpenter and B. Fridovich. Effect of a rapid blade-pitch increase on the thrust and induced-velocity response of a full-scale helicopter rotor. Technical Report Technical Note 3044, NACA, Langley Aeronautical Laboratory, Langley Field, Va., 1953.

C.-T. Chen. *Linear system theory and design*. Oxford University Press, New York, 4th international edition, 2014. ISBN 9780199964543.

R. P. Coleman, A. M. Feingold, and C. W. Stempin. Evaluation of the induced-velocity field of an idealized helicoptor rotor. Technical report, DTIC Document, 1945.

J. T. Conway. Analytical solutions for the actuator disk with variable radial distribution of load. *Journal of Fluid Mechanics*, 297:327–355, 1995.

R. E. Froude. On the part played in propulsion by difference in pressure. *Transaction of the Institute of Naval Architects*, 30:390–423, 1889.

Z. Gimbutas, L. Greengard, and M. Minion. Coulomb interactions on planar structures: inverting the square root of the laplacian. *SIAM Journal on Scientific Computing*, 22(6):2093–2108, 2001.

B. Gustavsen and A. Semlyen. Rational approximation of frequency domain responses by vector fitting. *IEEE Transactions on power delivery*, 14(3):1052–1061, 1999.

M. O. L. Hansen. *Aerodynamics of wind turbines*. Earthscan, London, second edition, 2008.

L. Hörmander. *The Analysis of Linear Partial Differential Operators I*, volume 256 of *Classics in Mathematics*. Springer Berlin Heidelberg, 2003.

W. Johnson. *Helicopter theory*. Dover Publications, New York, 1994.

W. Kinner. Über tragflügel mit kreisförmigem grundriß. *ZAMM-Journal of Applied Mathematics and Mechanics/Zeitschrift für Angewandte Mathematik und Mechanik*, 16(6):349–352, 1936.

N. Laskin. Fractional quantum mechanics and lévy path integrals. *Physics Letters A*, 268(4):298–305, 2000.

J. G. Leishman, M. J. Bhagwat, and A. Bagai. Free-vortex filament methods for the analysis of helicopter rotor wakes. *Journal of aircraft*, 39(5):759–775, 2002.

J. A. Morillo and D. A. Peters. Velocity field above a rotor disk by a new dynamic inflow model. *Journal of aircraft*, 39 (5):731–738, 2002.

S. Øye. Unsteady wake effects caused by pitch–angle changes. In *IEA R&D WECS Joint Action on Aerodynamics of Wind Turbines, 1st Symposium*, pages 58–79, 1986.

S. Øye. Tjæreborg wind turbine. 4. dynamic inflow measurements. AFM Notat VK 204, Department of fluid mechanics, DTH Lyngby, October 1991.

M. D. Pedersen. Steady and transient inflow dynamics with actuator disk vortex theory. *Wind Energy*, 22(1):124–139, 2019. Submitted for review 14 July 2015, Revised 7 april 2017, Accepted June 2018.

D. A. Peters and N. HaQuang. Dynamic inflow for practical applications. *Journal of the American Helicopter Society*, 33(4), 10 1988.

D. A. Peters, D. D. Boyd, and C. J. He. Finite-state induced-flow model for rotors in hover and forward flight. *Journal of the American Helicopter Society*, 34(4):5–17, 1989.

D. M. Pitt and D. A. Peters. Theoretical prediction of dynamic-inflow derivatives. *Vertica*, 5(1):21–34, 1981.

P. G. Saffman. *Vortex dynamics*. Cambridge monographs on mechanics and applied mathematics. Cambridge University Press, Cambridge, New York, first edition, 1995.

J. Sørensen, W. Shen, and X. Munduate. Analysis of wake states by a full-field actuator disc model. *Wind Energy*, 1 (2):73–88, 1998.

P. R. Spalart. On the simple actuator disk. *Journal of Fluid Mechanics*, 494:399–405, 2003.

E. M. Stein and G. Weiss. *Introduction to Fourier Analysis on Euclidian spaces*, volume 32 of *Princeton Mathematical Series*. Princeton University Press, Princeton, New Jersey, 1971.

I. S. Sullivan, J. J. Niemela, R. E. Hershberger, D. Bolster, and R. J. Donnelly. Dynamics of thin vortex rings. *Journal of Fluid Mechanics*, 609:319–347, 2008.

G. J. W. Van Bussel. *The aerodynamics of horizontal axis wind turbine rotors explored with asymptotic expansion methods*. PhD thesis, Technische Universiteit Delft, 1995.